

m-NLP inference models using simulation and regression techniques

Guangdong Liu^{1,1,1}, Sigvald Marholm^{2,2,2}, Anders Eklund^{3,3,3}, Lasse Boy Novock Clausen^{4,4,4}, and Richard Marchand^{1,1,1}

¹University of Alberta

²University Of Oslo

³SINTEF Industry

⁴University of Oslo

November 30, 2022

Abstract

Current inference techniques for processing multi-needle Langmuir Probe (m-NLP) data are often based on the Orbital Motion-Limited (OML) theory which relies on several simplifying assumptions. Some of these assumptions, however, are typically not well satisfied in actual experimental conditions, thus leading to uncontrolled uncertainties in inferred plasma parameters. In order to remedy this difficulty, three-dimensional kinetic particle in cell simulations are used to construct synthetic data sets, which are then used to train and validate regression-based models capable of inferring electron density and satellite potentials from 4-tuples of currents collected with fixed-bias needle probes similar to those on the NorSat-1 satellite. Based on our synthetic data, the techniques presented enable excellent inferences of the plasma density, and floating potentials, while the generally accepted OML inferred densities are approximately three times too high. The new inference techniques that we propose, are applied to NorSat-1 data, and compared with OML inferences. While both regression and OML based inferences of floating potentials agree well with synthetic data, only regression inferred potentials are consistent with satellite measured currents, indicating that the regression based inference models are more robust and accurate when applied to satellite data.

1 **m-NLP inference models using simulation and**
2 **regression techniques**

3 **Guangdong Liu¹, Sigvald Marholm^{2,3}, Anders J. Eklund⁴, Lasse Clausen²,**
4 **Richard Marchand¹**

5 ¹Department of Physics, University of Alberta, Edmonton, AB, Canada

6 ²Department of Physics, University of Oslo, Oslo, Norway

7 ³Department of Computational Materials Processing, Institute for Energy Technology, Kjeller, Norway

8 ⁴Materials Physics Oslo, SINTEF Industry, Oslo, Norway

9 **Key Points:**

- 10 • 3-D kinetic PIC simulations are used to simulate currents collected by m-NLP in
11 order to create a synthetic solution library
- 12 • Models to infer physical parameters from m-NLP measurements are constructed
13 and assessed on the basis of synthetic and in situ data sets
- 14 • Promising new approaches are identified to analyze m-NLP measurements based
15 on simulation and in-situ data

Corresponding author: Guangdong Liu, guangdon@ualberta.ca

Abstract

Current inference techniques for processing multi-needle Langmuir Probe (m-NLP) data are often based on adaptations of the Orbital Motion-Limited (OML) theory which relies on several simplifying assumptions. Some of these assumptions, however, are typically not well satisfied in actual experimental conditions, thus leading to uncontrolled uncertainties in inferred plasma parameters. In order to remedy this difficulty, three-dimensional kinetic particle in cell simulations are used to construct a synthetic data set, which is used to compare and assess different m-NLP inference techniques. Using a synthetic data set, regression-based models capable of inferring electron density and satellite potentials from 4-tuples of currents collected with fixed-bias needle probes similar to those on the NorSat-1 satellite, are trained and validated. The regression techniques presented show promising results for plasma density inferences with RMS relative errors less than 20 %, and satellite potential inferences with RMS errors less than 0.2 V for potentials ranging from -6 V to -1 V. The new inference approaches presented are applied to NorSat-1 data, and compared with existing state-of-the-art inference techniques.

1 Introduction

Langmuir probes are widely used to characterize space plasma and laboratory plasma. A variety of Langmuir probe geometries are being used, such as spherical (Bhattarai & Mishra, 2017), cylindrical (Hoang, Clausen, et al., 2018), and planar probes (Lira et al., 2019; Johnson & Holmes, 1990; Sheridan, 2010). Probes can be operated in sweep mode (Lebreton et al., 2006), harmonic mode (Rudakov et al., 2001), or fixed biased mode (Jacobsen et al., 2010), for different types of missions and measurements. Despite operational differences, all Langmuir probes consist of conductors exposed to plasma to collect current as a function of bias voltage. A common approach to infer plasma parameters from Langmuir probes is to sweep the bias voltage and produce a current-voltage characteristic, which can be analyzed using theories such as the Orbital Motion-Limited (OML) (Mott-Smith & Langmuir, 1926) theory, the Allen-Boyd-Reynolds (ABR) theory (Allen et al., 1957; Chen, 1965, 2003), and the Bernstein-Rabinowitz-Laframboise (BRL) theory (Bernstein & Rabinowitz, 1959; Laframboise, 1966) to obtain plasma parameters such as density, temperature, and satellite floating potential. The temporal and, on a satellite, the spatial resolution of Langmuir probe measurements are determined by the sweep time, which varies based on the mission's scientific need and available resources. Considering the orbital speed to be around 7500 m/s for a satellite in low Earth orbit (LEO), the spatial resolution of sweep bias Langmuir probe can vary from tens of meters, to kilometers, depending on the sweep frequency. In order to study the formation of density irregularities that scale from meters to tens of kilometers at high and low latitudes, a sampling frequency of near 1 kHz is required (Hoang, Røed, et al., 2018; Jacobsen et al., 2010). A solution, proposed by Jacobsen is to use multiple fixed biased needle probes (m-NLPs) to sample plasma simultaneously at different bias potentials in the electron saturation region (Jacobsen et al., 2010). This approach would eliminate the need for sweeping the bias voltage, and greatly increase the sampling rate of the instrument.

The first inference models for m-NLPs relied on the OML approximation, from which the current I_e collected by a needle probe in the electron saturation region is written as:

$$I_e = -n_e e A \frac{2}{\sqrt{\pi}} \sqrt{\frac{kT_e}{2\pi m_e}} \left(1 + \frac{e(V_f + V_b)}{kT_e} \right)^\beta, \quad (1)$$

where n_e is the electron density, A is the probe surface area, e is the elementary charge, k is Boltzmann's constant, T_e is the electron temperature, V_f is the satellite floating potential, V_b is the bias potential of the probe with respect to the satellite, and β is a parameter related to probe geometry, density, and temperature (Marholm & Marchand, 2020; Hoang, Røed, et al., 2018). Several assumptions were made in the derivation of this inference equation; such as the probe length must be much larger than the Debye length,

and the plasma is non-drifting. If these assumptions are valid, then $\beta = 0.5$, and as first suggested by Jacobsen, a set of m-NLPs can be used to infer the electron density independently of the temperature (Jacobsen et al., 2010). For a satellite in near-Earth orbit at altitudes ranging from 550 km to 650 km, we can expect a Debye length of around 2-50 mm, and an orbital speed of around 7500 m/s. A common length for m-NLP instrument used on small satellites is ~ 25 mm (Bekkeng et al., 2010; Hoang, Clausen, et al., 2018; Hoang et al., 2019), which is often comparable to, and sometimes smaller than the Debye length. In lower Earth orbit, ion thermal speeds are usually less than the orbital speed, while electron thermal speeds are usually higher than the orbital speed. Thus, the orbital speed is expected to mainly affect ion saturation region currents for Langmuir probes. However, electrons can only penetrate the ion rarefied wake region behind the probe as much as ambipolar diffusion permits (Barjatya et al., 2009). As a result, electron saturation currents are also influenced by an orbital speed. One consequence is that the $\beta = 0.5$ assumption does not hold in Eq. 1, and a better approximation for the current is obtained with β values between 0.5 and 1. For example, in a hot filament-generated plasma experiment, Sudit and Woods showed that β can reach 0.75 for a ratio between the probe length and the Debye length in the range of 1 to 3. For larger Debye lengths, they also observed an expansion of the probe sheath from a cylindrical shape into a spherical shape (Sudit & Woods, 1994). Ergun and co-workers showed that with a ram speed of 4300 m/s in their simulations, the current collected by a 40.8 cm needle probe is better approximated with Eq. 1 using a β value of 0.67 instead of 0.55 calculated in a stationary plasma (Ergun et al., 2021). In the ICI-2 sounding rocket experiment, β calculated from three 25 mm m-NLPs varied between 0.3 to 0.7 at altitudes ranging from 150 to 300 km (Hoang, Røed, et al., 2018). Simulation results by Marholm et al. showed that even a 50 mm probe at rest can be characterized by a $\beta \sim 0.8$ (Marholm et al., 2019), in disagreement with the OML theory. In practice, needle probes are mounted on electrically isolated and equipotential guards in order to attenuate end effects on the side to which they are attached. The distribution of the current collected per unit length is nonetheless not uniform along the probe, as more current is collected near the end opposite to the guard. A study by Marholm & Marchand showed that for a cylindrical probe length that is 10 times the Debye length, β is approximately 0.72. For a probe length that is 30 times the Debye length, β is approximately 0.62, and with a guard, this number is reduced to 0.58 (Marholm & Marchand, 2020). Although this number approaches 0.5, 30 times the Debye length is a stringent requirement for OML to be valid, and it is hardly ever fulfilled in practice. Experimentally, Hoskinson and Hershkowitz showed that even with a probe length 50 times the Debye length, β is approximately 0.6, and the density inference based on an ideal $\beta = 0.5$ is 25 % too high (Hoskinson & Hershkowitz, 2006). Barjatya estimated that even a 10% error in β (to 0.55) can result in a 30 % or more relative error in the calculated density based on the $\beta = 0.5$ assumption (Barjatya & Merritt, 2018). In what follows, we find that densities estimated using Eq. 1 assuming $\beta = 0.5$ are about three times larger than the known values used as input in our simulations, as illustrated in section 3.1. This is consistent with findings in (Barjatya & Merritt, 2018; Guthrie et al., 2021), considering β calculated in our simulation is in the range of 0.75 to 1. Another approach proposed to account for the fact that β is generally different from 0.5, consists of determining the n_e , V_b , T_e and β , as adjustable parameters in nonlinear fits of measured currents as a function of voltages. This led to remarkable agreement with density measured using a radio frequency impedance probe on the international space station (Barjatya et al., 2009, 2013; Debchoudhury et al., 2021). This method was originally applied to a probe operated in sweep voltage mode, but it can be straightforwardly adapted to fixed bias m-NLP measurements (Barjatya et al., 2009; Barjatya & Merritt, 2018; Hoang, Røed, et al., 2018).

In the following, we assess different techniques to infer plasma densities, and satellite potentials from fixed bias needle probe measurements based on synthetic data obtained from kinetic simulations. We also present a new method to interpret m-NLP measurements based on multivariate regression. Our kinetic simulation approach and the con-

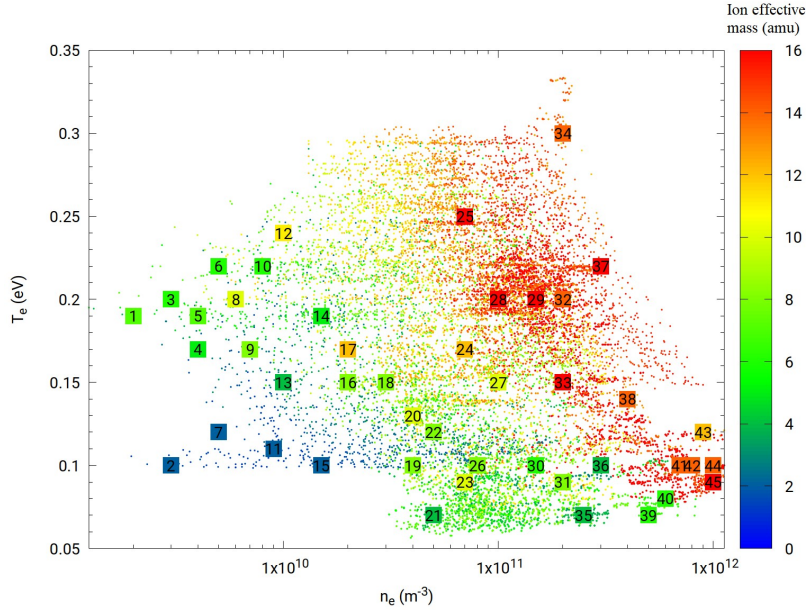


Figure 1. Scatter plot of plasma parameters obtained from the IRI model, corresponding to different latitudes, longitudes, altitudes, and times, as listed in Table 1. The x and y axes, and the color bar refer respectively, to the electron density, electron temperature, and the ion effective mass. Numbered squares identify the set of parameters used in the kinetic simulations.

121 construction of a synthetic data set are presented in Sec. 2. In Sec. 3, regression models are
 122 trained using synthetic data sets, and they are assessed using distinct validation sets.
 123 In Sec. 4, the same models are applied to NorSat-1 data, to infer densities and satellite
 124 potentials from in situ measured currents. Section 5 summarizes our findings and presents
 125 some concluding remarks.

126 2 Methodology

127 In this section, we briefly describe our kinetic simulation approach, and how it is
 128 used to construct synthetic data sets used to train and validate inference models, using
 129 two regression techniques. We then describe the various models to infer density, and satel-
 130 lite potential from m-NLP measurement.

131 2.1 Kinetic simulations

132 The space plasma parameters considered in our simulations are selected so as to
 133 be representative of conditions expected for a satellite in low Earth orbit at altitudes rang-
 134 ing between 550 and 650 km. This is done by sampling ionospheric plasma parameters
 135 using the International Reference Ionosphere (IRI) (Bilitza et al., 2014) model in a broad
 136 range of latitudes, longitudes, altitudes, and times as shown in Fig. 1. The ranges con-
 137 sidered for these parameters are summarized in Tab. 1. Forty-five sets of plasma param-
 138 eters approximately evenly distributed in this parameter space are selected as input in
 139 simulations, as shown in numbered squares in Fig. 1. The three-dimensional PIC code
 140 PTetra (Marchand, 2012; Marchand & Lira, 2017) is used to simulate probe currents in
 141 this study. Cross comparisons are made between PTetra simulation results and analytic
 142 results under conditions when those are valid, and with other independently developed
 143 simulation codes, and show excellent agreement (Deca et al., 2013; Marchand et al., 2014).

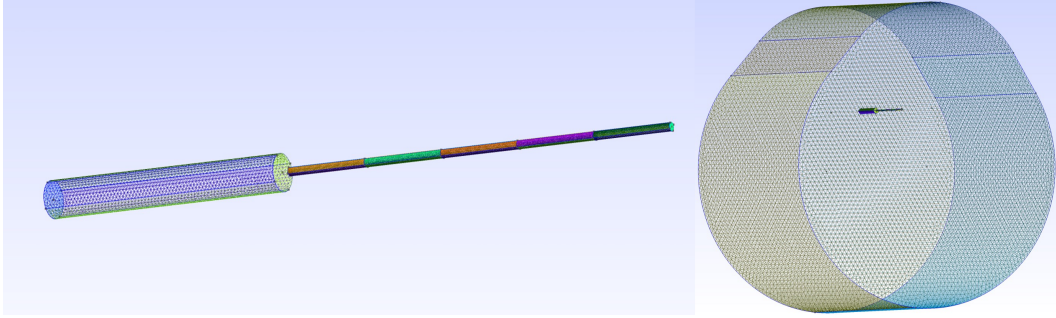


Figure 2. Illustration of a m-NLP geometry (left), and the simulation domain (right). The needle probe has a length of 25 mm and a radius of 0.255 mm, with a guard of 15 mm in length and 1.1 mm in radius. The ram flow is from the top of the simulation domain and is assumed to be 7500 m/s.

144 In PTetra, space is discretized using unstructured adaptive tetrahedral meshes (Frey &
 145 George, 2007; Geuzaine & Remacle, 2009). Poisson’s equation is solved at each time step
 146 using Saad’s GMRES sparse matrix solver (Saad, 2003) in order to calculate the elec-
 147 tric field in the system. Then, electron and ion trajectories are calculated kinetically us-
 148 ing their physical charges and masses self consistently. The mesh for the m-NLP and the
 149 simulation domain illustrated in Fig. 2, is generated with GMSH (Geuzaine & Remacle,
 150 2009). The needle probe used in the simulation has a length of 25 mm and a diameter
 151 of 0.51 mm, as those on the NorSat-1. The needle probe is attached to a 15 mm long
 152 and 2.2 mm diameter guard which is biased to the same voltage as the probe. The outer
 153 boundary of the simulation domain is closer to the probe on the ram side, and farther
 154 on the wake side, as shown in Fig. 2. The simulations are made using two different do-
 155 main sizes depending on the Debye length of the plasma. For plasma densities below $2 \times$
 156 10^{10} m^{-3} corresponding to a Debye length of 1.9-7.2 cm, a larger domain is used. For plasma
 157 densities above $2 \times 10^{10} \text{ m}^{-3}$, corresponding to a Debye length of 0.2-2.2 cm, a smaller
 158 domain with finer resolution is used. The simulation size, the resolution, the number of
 159 tetrahedra, and the corresponding Debye length are summarized in Tab. 2. There is over-
 160 lap between the two simulation domains for simulations with Debye lengths around 2
 161 cm. No obvious difference was found in the simulated currents, indicating that simula-
 162 tion results from both domains are consistent in the transition range. Simulation results
 163 from both domains are included when training the regression models. All simulations
 164 are run initially with 100 million ions and electrons, but these numbers vary through a
 165 simulation, due to particles being collected, leaving, or entering the domain. In the sim-
 166 ulations, the probe is segmented into five segments of equal lengths, making it possible
 167 to estimate a rough distribution of the current along its length. The current used to build
 168 regression models is a sum of the currents of the five different segments. The orbital speed
 169 of the satellite is assumed to be fixed at 7500 m/s in the simulations, with a direction
 170 perpendicular to the probe. For the voltages considered, probes are expected to collect
 171 mainly electron currents. For simplicity, only two types of ions are considered in the sim-
 172 ulation, O^+ and H^+ ions, and no magnetic field is accounted for, which is justified by
 173 the fact that the Larmor radius of the electron considered is much larger than the radi-
 174 us of the probe. The probes are assumed to be sufficient far on the ram side, away from
 175 other satellite components, to be unaffected by their presence. NorSat-1 satellite has a
 176 Sun synchronous orbit, thus is moving approximately parallel to the magnetic field near
 177 the equator. As a result, in these regions $\vec{V} \times \vec{B}$ should be small at low and mid mag-
 178 netic latitudes, and it is not accounted for in the simulations.

Table 1. Spatial and temporal parameters used to sample ionospheric plasma conditions in IRI, and the corresponding ranges in space plasma parameters.

Environment and plasma conditions	Parameter range
Years	1998 2001 2004 2009
Dates	Jan 4 Apr 4 Jul 4 Oct 4
Hours	0-24 with increment of 8 hours
Latitude	-90° - $+90^\circ$ with increment of 5°
Longitude	0° - -360° with increment of 30°
Altitude	550-650 km with increment of 50 km
Ion temperature	0.07-0.16 eV
Electron temperature	0.09-0.25 eV
Effective ion mass	2-16 amu
Density	$2 \times 10^9 - 1 \times 10^{12} \text{m}^{-3}$

Table 2. Parameters used in the two simulation domains are listed. The first two columns give the distances between the probe to the outer boundary on the ram side (D_{ram}), and the wake side (D_{wake}) respectively, followed by the simulation resolutions at the probe, guard, and the outer boundary. The number of tetrahedra used in the simulations is in the order of millions. The corresponding range in Debye lengths is also listed.

D_{ram}	D_{wake}	Probe resolution	Guard resolution	Boundary resolution	Tetrahedra	Debye length
3.5 cm	7 cm	51 μm	220 μm	2 mm	2.5 M	0.2-2.2 cm
30 cm	40 cm	51 μm	220 μm	1 cm	1.7 M	1.9-7.2 cm

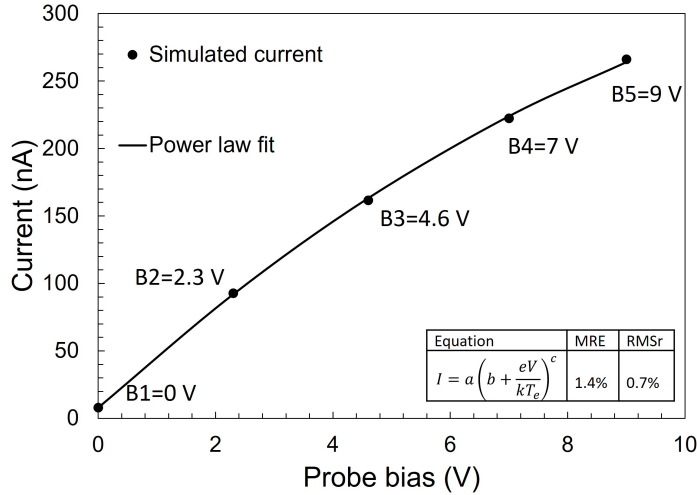


Figure 3. Comparison between calculated currents from PIC simulations, and fitted values using Eq. 6, assuming a density of $2 \times 10^{10} \text{m}^{-3}$, an effective mass of 8 amu, an electron and ion temperatures of 0.15 and 0.12 eV respectively, corresponding to point 16 in Fig. 1. The fitting errors in the figure are calculated over all 45 sets of plasma conditions using Eq. 3 and 5.

179

2.2 Synthetic solution library

180

181

182

183

In order to assess the inference skill of a regression model, a cost function is defined with the following properties: i) it is non-negative, ii) it vanishes if model inferences agree exactly with known data in a data set, and iii) it increases as inferences deviate from actual data. The cost functions used in this work are: the root mean square error,

184

$$RMS = \sqrt{\frac{1}{N_{data}} \sum_{i=1}^{N_{data}} (Y_{mod_i} - Y_{data_i})^2}, \quad (2)$$

185

the root mean square relative error

186

$$RMSr = \sqrt{\frac{1}{N_{data}} \sum_{i=1}^{N_{data}} \frac{(Y_{mod_i} - Y_{data_i})^2}{Y_{mod_i}^2}}, \quad (3)$$

187

the maximum absolute error

188

$$MAE = \max \{|Y_{mod} - Y_{data}|\}, \quad (4)$$

189

and the maximum relative error

190

$$MRE = \max \left\{ \left| \frac{Y_{mod} - Y_{data}}{Y_{mod}} \right| \right\}, \quad (5)$$

191

192

where Y_{data} and Y_{mod} represent respectively known and inferred plasma parameters, and N_{data} is the total number of data points.

193

194

195

For each of the 45 sets of plasma conditions corresponding to squares in Fig. 1, 5 simulations are made assuming 5 probe voltages with respect to background plasma, and the simulated currents vs probe voltage are fitted analytically with:

196

$$I = a \left(b + \frac{eV}{kT_e} \right)^c, \quad (6)$$

197

198

199

200

201

202

203

204

205

206

207

208

209

210

211

212

213

214

215

216

217

218

where a , b , and c are adjustable fitting parameters. The MRE calculated for the 45 fits is 1.4%, and the RMSr is 0.7%, which shows excellent agreement with simulated collected currents. A comparison between fitted and computed currents is shown in Fig. 3. The NorSat-1 m-NLP probes fixed biases V_b are +10, +9, +8, and +6 V, and the probe voltage with respect to background plasma is given by the sum of the spacecraft floating potential and the probe bias $V = V_f + V_b$. In simulations, probe currents calculated for voltages with respect to background plasma in the range between 0 to 9 volts are considered as shown in Fig. 3. Considering the probe bias voltages V_b given above, probe currents can be determined, corresponding to arbitrary floating potentials between -1 V and -6 V. A synthetic solution library is created for randomly distributed spacecraft floating potentials in the range between -1 and -6 V with corresponding currents obtained by interpolation using Eq. 6 with the fitting parameters computed for each of the 45 cases considered. The result is a synthetic solution library consisting of four currents collected by the four needle probes at the four different bias voltages, for 160 randomly distributed spacecraft potentials in the range between -1 V to -6 V for each of the 45 sets of plasma parameters. In each entry of the data set, these four currents are followed by the electron density, the spacecraft potential the electron and ion temperatures, and the ion effective mass as listed in Tab. 3. The resulting solution library consisting of $45 \times 160 = 7200$ entries is then used to construct a training set with 3600 randomly selected nodes or entries, and a validation set with the remaining 3600 nodes. The cost functions reported in what follows, used to assess the accuracy of inferences, are all calculated from the validation data set unless stated otherwise.

219

2.3 Multivariate regression

220

221

222

In a complex system where the relation between independent variables and dependent variables cannot readily be cast analytically, multivariate regressions based on machine learning techniques are powerful alternatives to construct approximate inference

Table 3. Example entries of the synthetic data set, with currents I_1 , I_2 , I_3 , and I_4 calculated using Eq. 6, and V_b set to 10, 9, 8, and 6 V, respectively. The floating potential V_f is selected randomly in the range of -1 to -6 V, and the probe voltages with respect to background plasma are given by $V = V_b + V_f$. The coefficients, a, b and c are obtained from a nonlinear fit of the simulated currents using Eq. 6. The first and second entries correspond respectively to points 16 and 21 in Fig. 1.

$I_1(nA)$	$I_2(nA)$	$I_3(nA)$	$I_4(nA)$	$V_f(V)$	$n_e(m^{-3})$	$T_e(eV)$	$T_i(eV)$	$m_{eff}(amu)$
233	208	183	129	-2.50	2×10^{10}	0.15	0.12	8
596	533	467	323	-2.93	5×10^{10}	0.07	0.07	4

223 models. In this approach, the model must be capable of capturing the complex relation-
 224 ship between dependent and independent variables. Once the model is trained using the
 225 training set, it can then be used to make inferences for cases not included in the train-
 226 ing data set. In this work, two multivariate regression approaches are used to infer plasma
 227 parameters: the Radial Basis Function and Feedforward Neural Networks. The models
 228 are trained by minimizing their cost function on the training data set, and then applied
 229 to the validation data set to calculate the validation cost function without further op-
 230 timization. The use of a validation set is to avoid “overfitting” because there are certain
 231 limitations on the refinement of a model on a training set, such that further improve-
 232 ment of model inference skill in the training set will worsen the model inference skill in
 233 the validation set. A good model is one with the right level of training so as to provide
 234 the best inference skill in the validation set.

2.3.1 Radial basis function

235
 236 Radial basis function (RBF) multivariate regression is a simple and robust tool used
 237 in many previous studies to infer space plasma parameters using a variety of instruments
 238 with promising results (Liu & Marchand, 2021; Olowookere & Marchand, 2021; Chalaturnyk
 239 & Marchand, 2019; Guthrie et al., 2021). A general expression for RBF regression for
 240 a set of independent n-tuples \bar{X} and corresponding dependent variable Y is given by:

$$241 \quad Y = \sum_{i=1}^N a_i G(|\bar{X} - \bar{X}_i|). \quad (7)$$

242 In general, the dependent variable Y can also be a tuple, but for simplicity, and with-
 243 out loss of generality, we limit our attention to scalar dependent variables. In Eq. 7, the
 244 \bar{X}_i represents the N centers, G is the interpolating function, and the a_i are fitting col-
 245 location coefficients which can be determined by requiring collocation at the centers; that
 246 is, by solving the system of linear equations

$$247 \quad \sum_{i=1}^N a_i G(|\bar{X}_k - \bar{X}_i|) = Y_k \quad (8)$$

248 for $k = 1, \dots, N$. Here, the dependent variable Y corresponds to the physical param-
 249 eter to be inferred, and the independent variable \bar{X} is a 4-tuple corresponding to the cur-
 250 rents or the normalized currents from the m-NLPs depending on which physical param-
 251 eters are being inferred. There are different ways to distribute the centers in RBF re-
 252 gression. One straightforward approach is to select centers from the training data set,
 253 and evaluate the cost function over the entire training data set for all possible combi-
 254 nations of centers, then select the model which yields the optimal cost function. For this

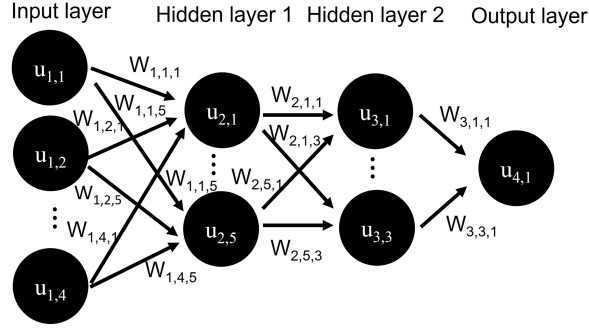


Figure 4. Schematic of a feedforward neural network.

255 approach, the number of combinations required for \mathcal{N} data points and N centers is given
 256 by

$$257 \quad \binom{\mathcal{N}}{N} = \frac{\mathcal{N}!}{N!(\mathcal{N} - N)!}. \quad (9)$$

258 This, of course, can be prohibitively large and time-consuming for a large training data
 259 set or using a large number of centers. An alternative strategy is to successively train
 260 models with randomly selected small subsets of the entire training data set using the straight-
 261 forward approach, while calculating the cost function on the full training set, and then
 262 carrying the optimal centers from one iteration to the next. This “center-evolving strat-
 263 egy” is very efficient in finding near-optimal centers for large training data sets and has
 264 proven to be as accurate as the straightforward extensive approach (Liu & Marchand,
 265 2022). The RBF models here follow this procedure. Different G functions and cost func-
 266 tions are tested, and only the models that yield optimal results are reported in this pa-
 267 per.

268 **2.3.2 Feedforward neural network**

269 The second multivariate regression approach is a Feedforward neural network as
 270 illustrated in Fig. 4. This consists of an input layer, hidden layers, and an output layer.
 271 Each node j in a given layer i in the network is assigned a value $u_{i,j}$, and the node in
 272 the next layer $i+1$ are “fed” from numerical values from the nodes in the previous layer
 273 according to

$$274 \quad u_{i+1,k} = f \left(\sum_{j=1}^{n_i} w_{i,j,k} u_{i,j} + b_{i,k} \right), \quad (10)$$

275 where $w_{i,j,k}$ are weight factors, $b_{i,j}$ are bias terms, and f is a nonlinear activation func-
 276 tion (Goodfellow et al., 2016). In this work, the input layer neurons contain the four-
 277 needle probe currents or normalized currents depending on the physical parameter to
 278 be inferred, whereas the output layer contains one physical parameter. The number of
 279 hidden layers and the number of neurons in the hidden layers are adjusted to fit the spe-
 280 cific problem, and attain good inference skills. The Feedforward neural network is built
 281 using TensorFlow (Abadi et al., 2016) with Adam optimizer (Kingma & Ba, 2015), and
 282 using the ReLU activation function defined as $f(x) = \max(0, x)$. The input variables
 283 are normalized using the `preprocessing.normalization` TensorFlow built-in function
 284 which normalizes the data to have a zero mean and unit variance. The structure of the
 285 network will be described later when presenting model inferences.

286

2.4 Space plasma and satellite parameter inference models

287

288

289

The next step is to construct models that maps the measured currents to the corresponding plasma and satellite conditions in the solution library. Various models used to infer plasma densities and satellite potentials are described in this section.

290

2.4.1 Density inference

291

292

293

The density can be inferred directly from the above two multivariate regression models using the currents collected by the four probes as inputs. The density can also be inferred using Eq. 1 which can be rewritten as

294

$$\frac{n_e}{T_e^{\beta-\frac{1}{2}}} = \sqrt{\frac{\pi^2 m_e}{2A^2 e^3}} \left(\frac{I_1^{\frac{1}{\beta}} - I_2^{\frac{1}{\beta}}}{V_1 - V_2} \right)^\beta. \quad (11)$$

295

296

297

In this equation, subscripts 1 and 2 indicate different probes. A special case of this equation was first proposed by Jacobsen, assuming an infinitely long probe, for which $\beta = 0.5$, resulting in

298

$$n_e = \sqrt{\frac{\pi^2 m_e}{2A^2 e^3}} \sqrt{\frac{I_1^2 - I_2^2}{V_1 - V_2}}, \quad (12)$$

299

300

301

302

303

304

305

306

307

308

309

310

311

which gives an expression for the electron density, independently of the temperature (Jacobsen et al., 2010). With currents from more than two probes, the density can be calculated from the slope of the current squared as a function of the bias voltage from a linear least-square fit of all probes (Jacobsen et al., 2010). This will be referred as the ‘‘Jacobsen linear fit’’ (JLF) approach. It is now well known however, that for finite length probes, with lengths not much larger than the Debye length, β typically ranges between 0.6 and 1. This is the case in particular for the needle probes on NorSat-1 with ratios between probe lengths to Debye length ranging from 0.5 to 12.5. As a consequence, when this method is applied to the solution library, the inferred density is typically three times larger than the density used in the simulation as shown with red boxes in Fig 5. Analytic inferences can be improve by adopting a boosting strategy. With this approach, the less accurate analytic model is used as a first approximation, which is then corrected by applying a more advanced regression technique.

312

313

314

315

316

317

Two boosting strategies are used in this study, consisting of i) an affine transformation, and b) RBF. Considering that the Pearson correlation coefficient R is invariant under an affine transformation, it follows that the offset between two data set, with a high value of R , can be significantly reduced with a simple affine transformation. To be specific, in this case, the density is first approximated using the JLF approach, and an affine transformation is applied to the natural log of the density as in:

318

$$\ln(n_e^{\text{affine}}) = a \ln(n_e^{\text{JLF}}) + b. \quad (13)$$

319

320

321

322

where a and b are determined with a simple least square fit to the known log of the densities in the data set. In the second approach, RBF is used to model the discrepancy between the JLF approximated density and the known densities, and the modeled discrepancy is used to correct the first JLF estimate.

323

324

325

326

327

328

329

330

331

The nonlinear least square fit proposed by Barjatya is also used to infer the density and the satellite potential. In their paper, Barjatya, et al. (Barjatya et al., 2009) apply this method to a full characteristic, covering the ion saturation, the electron retardation, and electron saturation regions. This enabled them to infer all four parameters in Eq. 1, namely, n_e , T_e , V_f , and β . In our analysis, inferences are made from only four currents from four probes at fixed bias voltages, all in the electron saturation region. As shown by Barjatya and Merritt (Barjatya & Merritt, 2018), however, it is difficult to infer the temperature using this approach, owing to the weak dependence of collected currents on the electron temperature (see Eq. 11). A solution, proposed in (Barjatya

332 & Merritt, 2018; Hoang, Røed, et al., 2018), then consists of estimating the electron tem-
 333 perature from other measurements, or from the IRI model, and perform the fit for the
 334 remaining three parameters. This simplification is justified by the fact that, following
 335 this procedure, a 50% error in the temperature, still produces acceptable results for the
 336 other parameters (Barjatya & Merritt, 2018). Thus unless stated otherwise, we assume
 337 a fixed electron temperature (~ 2000 K), which is in the middle of the temperature range
 338 considered in the simulations, and fit 4-tuples of currents using V_f , n_e , and β values as
 339 fitting parameters. This “Barjatya nonlinear fit” (BNLF) approach will be used to in-
 340 fer both density and potential from a set of measurement.

341 **2.4.2 Analytic estimate of V_f**

342 The satellite potential can be inferred directly from the currents using RBF regres-
 343 sion. In this approach, the four currents are normalized by dividing every current by their
 344 sum, in order to remove the strong density dependence on the currents. A neural net-
 345 work does not produce satisfactory in this case, and it is not used to infer the satellite
 346 potential. The floating potential of the spacecraft can also be inferred using the OML
 347 equation, by rewriting equation 1 as:

$$348 \quad V_f \approx V_f + \frac{kT_e}{e} = \frac{V_2 I_1^{\frac{1}{\beta}} - V_1 I_2^{\frac{1}{\beta}}}{I_2^{\frac{1}{\beta}} - I_1^{\frac{1}{\beta}}} = \frac{V_3 I_2^{\frac{1}{\beta}} - V_2 I_3^{\frac{1}{\beta}}}{I_3^{\frac{1}{\beta}} - I_2^{\frac{1}{\beta}}}. \quad (14)$$

349 In this equation, the subscripts 1,2, and 3 refer to different probes, thus there must be
 350 at least three probes in order to solve for β . The bias voltages of the probes and their
 351 corresponding collected currents are known from measurements, thus β can be solved
 352 using a standard root finder. Given β , equation 14 then provides a value for $V_f + \frac{kT_e}{e}$.
 353 In this expression, $\frac{kT_e}{e}$ is the electron temperature in electron-volt, which in the lower
 354 ionosphere at mid latitudes, is of order 0.3 eV or less. Thus, considering that $\frac{kT_e}{e}$ is gen-
 355 erally much smaller than satellite potentials relative to the background plasma, any of
 356 the two terms in the right side of Eq. 14 provides a first approximation of V_f (Guthrie
 357 et al., 2021). This will be referred to as the “adapted OML” approach.

358 **3 Assessment with synthetic data**

359 In this section, we assess our models using synthetic data, which allows us to check
 360 the accuracy, and quantify uncertainties in our inferences. A consistency check strategy
 361 is also introduced to further assess the applicability of our models.

362 **3.1 Density and satellite potential inference**

363 Direct RBF regression is applied to infer the density using the four currents as in-
 364 put variables. When constructing an RBF model with $G(x) = |x|$, minimizing MRE,
 365 and using 6 centers, the RMSr and MRE calculated on the validation data set are 17%
 366 and 35%, respectively. A test is made to infer the density using RBF with 35 randomly
 367 selected entries from the 45 plasma conditions in the solution library. With 30 voltages,
 368 and the same G function, cost function and number of centers, the calculated MRE is
 369 also 35 %. This is an indication that 45 sets of plasma conditions and 160 voltages should
 370 be sufficient in terms of sampling size to construct regression models. Using a neural net-
 371 work with 4 nodes in the input layer, 14 nodes and 12 nodes in two hidden layers, and
 372 1 node in the output layer, results in a 14% RMSr and 43% MRE for the inferred den-
 373 sities. This is calculated using TensorFlow with ADAM optimizer with a learning rate
 374 of 0.005 and an RMSr as a cost function. The input layer is normalized to have a zero
 375 mean and unit variance, while the output layer is normalized by dividing by the largest
 376 density. The densities calculated using the synthetic solution library, as well as the cost
 377 function are shown in Fig. 5.

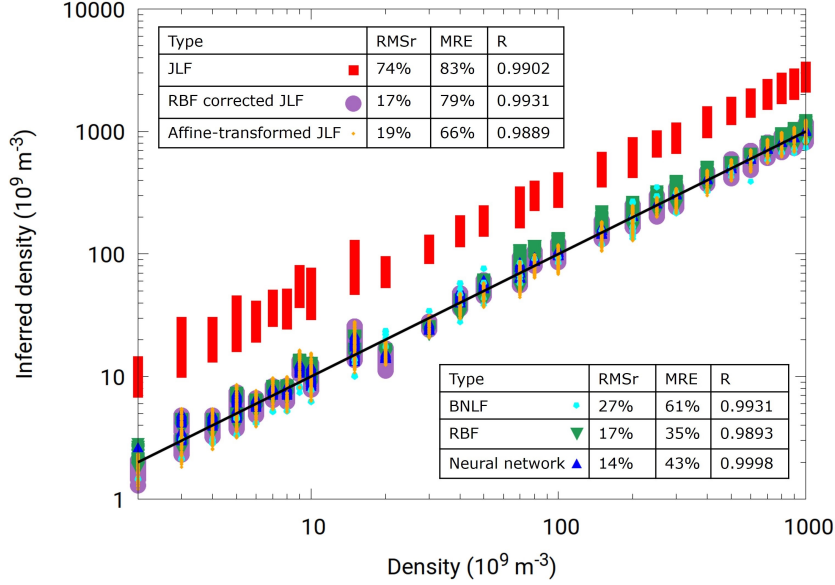


Figure 5. Correlation plot for the density inferences made with different techniques applied to our synthetic validation set. The Pearson correlation coefficient R is calculated using the inferred densities and the density used in the simulation. Black line represent idealized perfect correlation line.

378 When using an affine transformation to boost the JLF method, the coefficients a
 379 and b in Eq. 13 are obtained from a least-squares fit of the log of these densities, to those
 380 in the training data set. The fitting coefficients in this case, $a = 1.13261$ and $b = -4.82735$,
 381 are then used to perform an affine transformation on the validation data set, leading to
 382 a significant improvement in RMSr from 74% to 19%, and in MRE from 83% to 66% com-
 383 pared to densities inferred from the JLF approach, as shown in Fig 5. When boosting
 384 JLF density with RBF, the 4-tuple of currents is used as input variable \vec{X} . Minimizing
 385 the MRE using $G(x) = |x|$, and 5 centers, the RBF corrected JLF density yields an RMSr
 386 of 17 % and a MRE of 79%. The cost functions of the two boosting methods are com-
 387 parable, but an obvious advantage of using an affine transformation is its simplicity.

388 The Python 3 `LMFIT` package is used to do the nonlinear fit for the BNLF approaches
 389 as in (Debchoudhury et al., 2021). In the fits, the initial values for the density, the po-
 390 tential and the β value are $5 \times 10^{10} \text{ m}^{-3}$, -3 V and 0.85 , and the lower and upper bounds
 391 are 1×10^9 to $1 \times 10^{12} \text{ m}^{-3}$, -6 to -1 V , and 0.7 to 1 , respectively. The potential lower
 392 bound of -6 V is needed to ensure that the values under exponent in Eq. 1 are positive.
 393 We obtain 3600 fits for each of the 3600 entries of four currents in our validation data
 394 set. The fit minimizes RMSr as the cost function, and the overall RMSr calculated us-
 395 ing Eq. 3 for the 3600×4 currents is 0.2 %, and only 1.7% of the points have relative
 396 errors larger than 1%. The resulting density inferences have an RMSr of 27 % and a MRE
 397 of 61 %, which is better than the densities inferred from the JLF approach, but less ac-
 398 curate than those from the multivariate regression models. The β values calculated are
 399 in the range of 0.75 to 1. Using `LMFIT`, approximately 160 sets of currents can be fitted
 400 in one second using an AMD 5800x processor. In comparison, linear fits of the currents
 401 square, followed by an affine transformation of the log of the inferred density can be done
 402 using fixed formulas (7400 sets can be fitted in one second using an AMD 5800x), and
 403 thus are considerably faster than a nonlinear fit. Regression methods such as RBF or
 404 neural network are also numerically very efficient, considering they involve simple arith-
 405 metic expressions with pre-calculated coefficients. Compared to the other density mod-

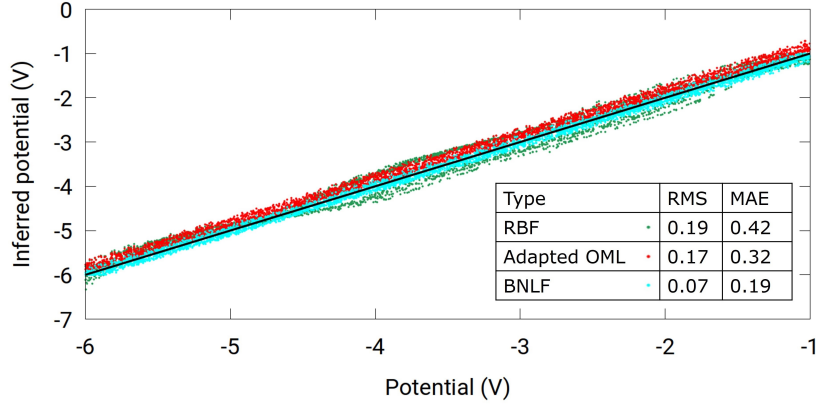


Figure 6. Correlation plot obtained for satellite potential inferred with RBF and OML techniques.

406 els considered, straightforward RBF yields the smallest MRE, thus it is the preferred model
 407 to infer density in this work. However, the affine-transformed JLF method enables den-
 408 sity inferences with accuracy comparable to those of more complex approaches. This sim-
 409 ple and practical technique should therefore be of interest in routine data analysis.

410 When the adapted OML approach is used to infer satellite potentials, a MAE of
 411 0.3 V is calculated using currents collected with probe biases of 10, 9, and 8 volts probes.
 412 Referring to Eq. 14, the error of 0.3 V is likely due in part to the maximum electron tem-
 413 perature of 0.3 eV considered in the simulations. The β values calculated in the synthetic
 414 solution library is in the range of 0.75 to 1. RBF regression is also used to infer satel-
 415 lite potentials. In this case, using $G(x) = |x|$, 5 centers, and minimizing the MAE, the
 416 calculated MAE on the validation data set is 0.4 V. The inferred satellite potential from
 417 the BNLF approach has an RMS of 0.07 V, and a MAE of 0.19 V, which proves this method
 418 to be the most accurate compared to the other methods considered. A correlation plot
 419 for potentials inferred using the RBF, adapted OML, and BNLF approaches is shown
 420 in Fig. 6. All methods show good agreement with values from the synthetic solution li-
 421 brary.

422 3.2 Consistency check

423 In order to further assess the applicability of our inference approaches, we perform
 424 the following consistency check. First, RBF models $M1(n_e)$ and $M1(V_f)$ are constructed
 425 to infer the density and satellite potential using 4-tuple currents from our synthetic data
 426 set. A second model ($M2$) is constructed to infer collected currents from densities and
 427 floating potentials in our synthetic data set. Since we are not able to infer temperatures
 428 from the currents, the temperature is not included in $M2$. Consistency is then assessed
 429 in two steps, by i) using currents from synthetic data and models $M1(n_e)$ and $M1(V_f)$
 430 to infer densities and floating potentials, and ii) applying models $M2$ to these inferred
 431 values, to infer back collected currents. RBF density and floating potential inferences
 432 are used in $M1(n_e)$, and $M1(V_f)$ as described in sec. 2.4. RBF is also used in $M2$ with
 433 $G(x) = \sqrt{1 + x^{2.5}}$, and minimizing RMSr with 5 centers. With perfect inference mod-
 434 els, the results for these back-inferred currents, should agree exactly with the starting
 435 currents from synthetic data. Variances between back-inferred and simulated currents
 436 in the synthetic data are presented as indicative of the level of confidence in our regres-
 437 sion techniques. The correlation plot in Fig. 7, shows back-inferred currents (green) cal-
 438 culated for a probe with 10 V bias against known currents from synthetic data. For com-

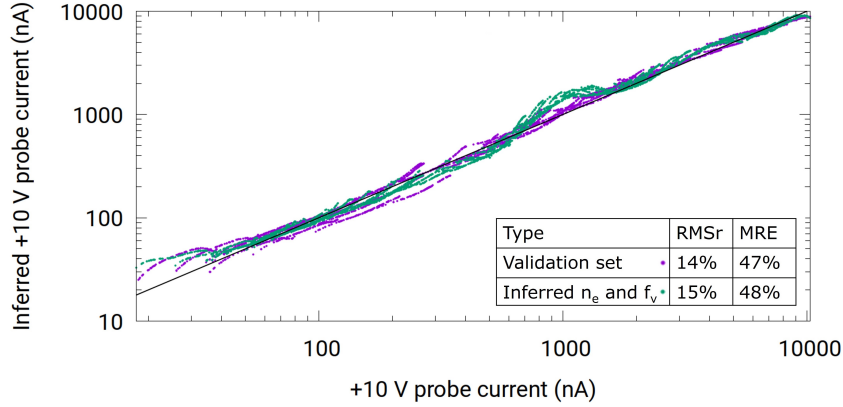


Figure 7. Correlation plot of inferred +10 V probe current against +10 V probe current from the synthetic data set. The calculated +10 probe currents in purple curve is calculated using the validation data set, while the green curve is calculated using inferred densities and floating potentials from RBF regression.

439 parison, the figure also shows the correlation between directly inferred currents (purple)
 440 when model M_2 is applied to densities and floating potentials in the synthetic data set.
 441 Both back-inferred and directly inferred currents are in excellent agreement with known
 442 currents from synthetic data, with comparable metric skills of $\simeq 15\%$ and $\simeq 48\%$
 443 for the RMSr and the MRE, respectively. Considering that errors are compounded between
 444 the first and second models for the back-inferred currents, the nearly identical metric skills
 445 in Fig. 7 is seen as confirmation of the validity of our regression models.

446 4 Application to NorSat-1 data

447 In this section, we apply our density and potential inference models constructed
 448 with synthetic data, to in situ measurements made with the m-NLP on the NorSat-1 satel-
 449 lite. The NorSat-1 currents were obtained from a University of Oslo data portal (Hoang,
 450 Clausen, et al., 2018). The epoch considered corresponds to one and a half orbit of the
 451 satellite starting at approximately 10:00 UTC on January 4, 2020. We start with a com-
 452 parison of simulated and measured currents to verify that our simulated currents are in
 453 the same range as those of measured in situ currents. Inferences made with RBF, neu-
 454 ral network, BNLF, adapted OML, and the two corrected JLF approaches constructed
 455 in 3.1, are also presented.

456 4.1 Measured in-situ, and simulated currents

457 The relevance of the space plasma parameter range considered in the simulations,
 458 to NorSat-1, is assessed in Fig. 8, by plotting currents collected by the +9 V probe against
 459 that collected by the +10 V, from both synthetic data, and in situ measurements. The
 460 close overlap, and the fact that the range of in situ measurements is within the range
 461 of simulated currents, indicates that the physical parameters selected in the simulations,
 462 are indeed representative to conditions encountered along the NorSat-1 orbit.

463 The current measurement resolution for the NorSat-1 m-NLP probes is approxi-
 464 mately 1 nA (Hoang, Clausen, et al., 2018). The noise level from the environment, how-
 465 ever, is estimated to be of order 10 nA. In what follows, darker colors are used to rep-
 466 resent inferences made using currents above 10 nA, and lighter colors are used to rep-
 467 resent inferences using currents between 1 to 10 nA. This is done by filtering out all data

468 that contain a current that is below 10 nA or 1 nA in any of the four probes. A word
 469 of caution is in order, however, for inferences made from these lower currents, as a con-
 470 servative estimate of the threshold for sufficient signal-to-noise ratios, is approximately
 471 10 nA. This lower bound current is supported by a consistency check made with mod-
 els 1 and 2 described in Sec. 3.2, and presented below in Sec. 4.3.

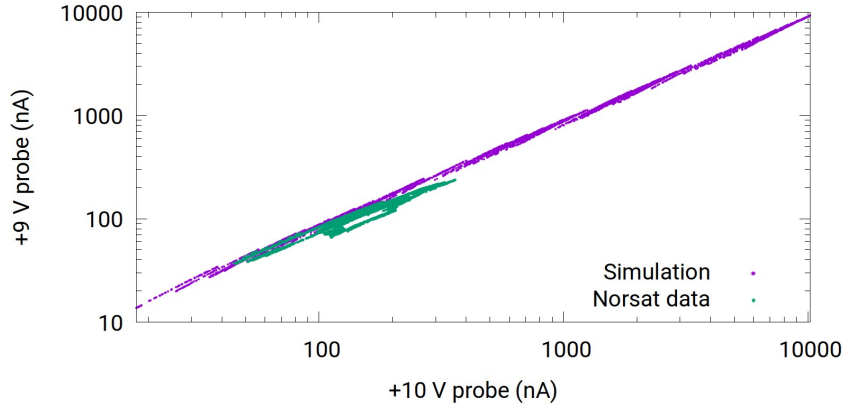


Figure 8. Correlation plot between currents collected by the +9 V and the +10 V probes for both NorSat-1, and synthetic data.

472

473 4.2 Density and satellite potential inference

474 Our models, trained with synthetic data as described in Sec. 3, are now applied
 475 to infer plasma densities and satellite potentials from in situ measured currents, for the
 476 time period considered. The results obtained with the different models presented in Sec.
 477 3 are shown in Fig. 9 for the inferred densities, satellite potentials, and measured cur-
 478 rents collected by the four probes. The position of the satellite relative to the Earth and
 479 the Sun given by the solar zenith angle, is also plotted in the figure. For example, a small
 480 solar zenith angle means that the satellite is near the equator on the dayside.

481 Applying the BNLF method with only four probes at fixed bias voltages, all in the
 482 electron saturation region, is more challenging than applying the technique to a probe
 483 operated in sweep mode, covering the ion saturation, the electron retardation, and the
 484 electron saturation regions. The reason is that in sweep mode, characteristics contain
 485 much more information than in fixed bias mode, with only four probes. In practice, in-
 486 ferences made from sweep mode characteristics are less sensitive to random errors in the
 487 currents, which, owing to their larger numbers, tend to cancel. With only four currents,
 488 however, noise is less likely to cancel, and inferences will be more sensitive to errors or
 489 noises, in measured currents. For example, the +8 V NorSat-1 probe currents are often
 490 slightly lower than expected for a downward concavity in I as a function of V_b , and tend
 491 to produce an upward concavity with β larger than 1. In this case, fitting the 4-tuples
 492 of currents using Eq. 1, for the density, the floating potential and β , with a specified elec-
 493 tron temperature is not practical. Thus we used a fixed β value of 0.85, and fit only den-
 494 sity and potential to the 4-tuples of currents using Eq. 1. This choice for the value of
 495 β is justified by the fact that it produces the best inferences when applied to synthetic
 496 data, with an RMS error of 0.41 V for the floating potential, and an RMSr error of 27
 497 % for the density. Based on comparisons made with our synthetic data sets, the use of
 498 a fixed β value results in a small loss in the inference accuracy for the satellite poten-
 499 tial, but the accuracy of the inferred density is the same as when β is included as a third
 500 fitting parameter. Using the fixed values of 0.172 eV for the electron temperature, and

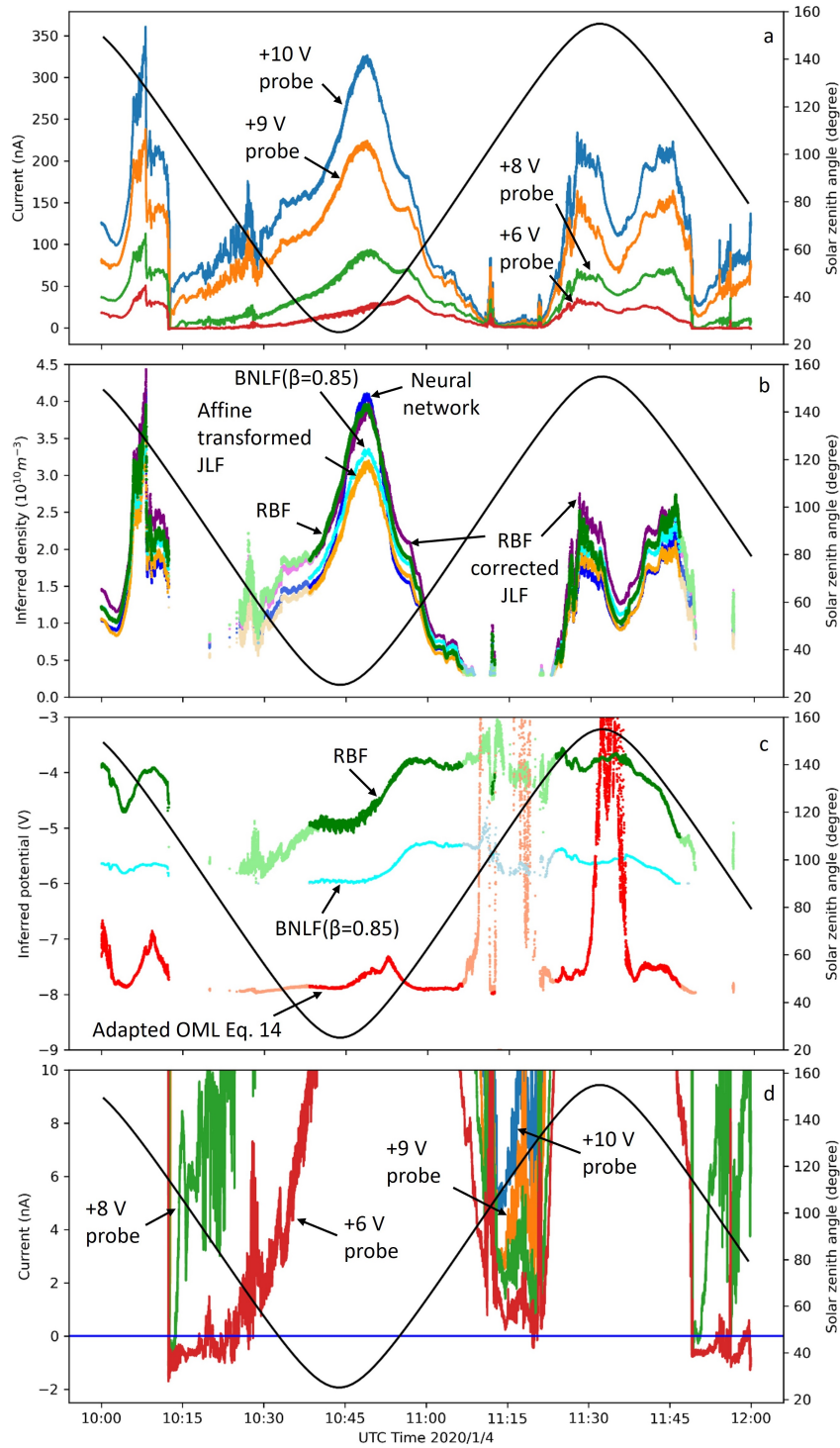


Figure 9. Illustrations of NorSat-1 collected currents considered in this study in panel a, inferred densities in panel b, inferred potentials in panel c, and the NorSat-1 current near 0 A in panel d. The solar zenith angle is also plotted against the secondary axis. Curves in darker colors are from model inferences using data above 10 nA, whereas those in lighter colors show inferences using data with currents between 1 nA and 10 nA.

501 0.85 for β , the RMSr error in the fits of the measured in situ currents, is 9%. The re-
 502 sulting inferred densities and satellite potentials are shown in Fig. 9. For reasons men-
 503 tioned above, it is clear that no satellite potential below the fitting lower bound of -6
 504 V can appear in the plot.

505 The densities shown in Fig. 9 panel b are obtained using the five density inference
 506 methods mentioned in Sec. 3.1. At 10:45, the neural network density, the RBF corrected
 507 JLF density, and the RBF density overlap nicely, while the affine transformed JLF den-
 508 sity and the BNLF density ($\beta = 0.85$) are smaller than other inferred densities, par-
 509 ticularly near the density maxima. The density inferences nonetheless qualitatively agree
 510 with each other. Using the +10, +9, and +8 NorSat-1 probe currents and Eq. 14, the
 511 inferred satellite floating potential is about -8 V for most of the data range considered
 512 in this study as shown in Fig. 9 panel c. This is in stark contradiction with observations
 513 in Fig. 9 panel d, which shows that the $+6$ V biased probe collects net positive electrons
 514 during most of the period considered. Also, there are periods between 10:15 to 10:30,
 515 and after 11:45 when the $+6$ V probe collects ion current (negative), indicating drops in
 516 the satellite potential below -6 V. The poor performance of Eq. 14 to infer the satellite
 517 potential here, results from the fact that Eq. 14 yields erratic values of β ranging from
 518 0.3 to 1.2. Attempts have also been made to approximate the satellite potential with Eq.
 519 14 using a fixed value of 0.58 and 0.78 for β , also resulting in satellite potentials in the
 520 -8 V range, and no improvement was found. This failure to produce acceptable values
 521 of the satellite potential clearly shows that the generalized OML expression in Eq. 14 does
 522 not provide a sufficiently accurate approximation for the currents collected by the NorSat-
 523 1 probes.

524 The RBF inferred floating potential shown in Fig. 9, is within -4 and -6 V, which
 525 is consistent with the observation that the $+6$ V probe collects electrons during most of
 526 the time period considered. This potential is generally lower than the potential estab-
 527 lished by the spacecraft on its own, likely due to the large number of electrons collected
 528 by the positively biased solar panels (Ivarsen et al., 2019). Interestingly, the inferred satel-
 529 lite potential using currents between 1 and 10 nA (light color) is seen to join smoothly
 530 with the darker color inferences, and to decrease below -6 V around 10:25, which is con-
 531 sistent with the observation that during that time the $+6$ V probe no longer collects elec-
 532 tron current. The floating potentials inferred from the BNLF model are systematically
 533 lower than those from RBF, and they also fit within the acceptable range for the satel-
 534 lite potentials. The two potentials have otherwise a very similar time dependences, and
 535 they are consistent with the fact that the $+6$ V probe collects zero net current near 10:25
 536 in panel d. The BNLF potential is bounded by the fitting lower limit of -6 V at these
 537 ranges, as opposed to RBF with which inferences are made without imposing an upper
 538 or lower bound. The currents collected by the probes are determined mostly by the den-
 539 sity and the satellite potential, and to a lesser extent, by the electron temperature. In
 540 Fig. 9, the density and floating potential are seen to peak at around 10:45 and 11:00 re-
 541 spectively. The currents from the +8, +9, and +10 V probes (green, orange, and blue)
 542 peak around 10:45, coinciding with the peak in the plasma density at this time. Then,
 543 as time goes forward to 11:00, the currents of the three probes decrease, also coinciding
 544 with a decrease in plasma density. However, the $+6$ V probe (red) current is increasing
 545 during these times, possibly due to an increase in floating potential. This increase is cap-
 546 tured in the RBF and BNLF inferred potential, but not in the one derived from adapted
 547 OML. Another observation is that the inferred floating potential decreases significantly
 548 at 10:15, as the satellite crosses the terminator. On NorSat-1, the negative terminals of
 549 the solar cells are grounded to the spacecraft bus while the positive side is facing the am-
 550 bient plasma (Ivarsen et al., 2019). A likely explanation for the potential drop is that
 551 the solar cells facing the ambient plasma get charged positively and suddenly start col-
 552 lecting more electrons upon exiting solar eclipse. This would agree with findings reported
 553 by Ivarsen et al. (Ivarsen et al., 2019).

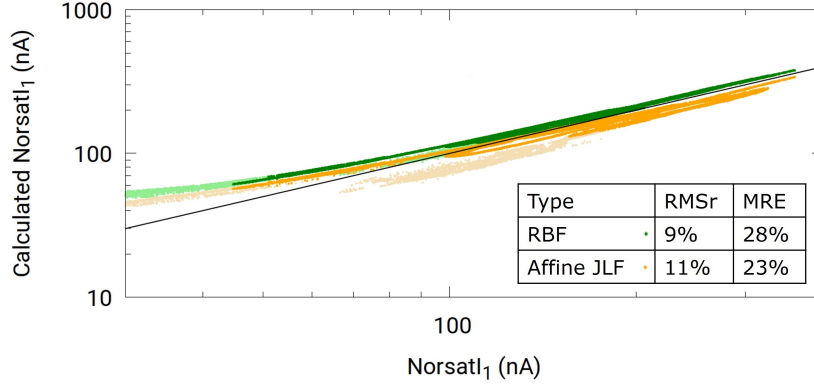


Figure 10. Consistency check is performed in the in situ data following the same procedure as in the synthetic data set. Both models 1 and 2 are trained with our synthetic data, and applied to currents from the +10 V probe on NorSat-1. Darker colors refer to inferences made with currents above 10 nA, while lighter colors refer to inferences obtained with currents between 1 and 10 nA.

554

4.3 Consistency check

555

556

557

558

559

560

561

562

563

564

565

566

567

568

569

570

571

572

573

574

575

576

577

578

579

580

581

582

In the absence of accurate and validated inferred densities and satellite potentials from NorSat-1 data, it is not possible to confidently ascertain to what extent the inferences presented above are accurate. As an alternative, we proceed with a consistency check, following the same procedure as presented in Sec. 3.2 with synthetic data, but using measured currents as input. This is done by first applying models $M1(n_e)$ and $M1(V_f)$ trained with synthetic data, to infer floating potentials and densities from measured currents. Then $M2$ (also trained with synthetic data) is used to infer currents from the $M1$ - inferred floating potentials and densities. If the models constructed from the synthetic data also apply to NorSat-1 data, the inferred currents should closely reproduce the measured NorSat-1 currents. A correlation plot of inferred against measured currents is shown in Fig. 10 for the +10 V probe. In this plot, the orange and green curves show back-inferred currents obtained with the RBF $M2$ model. For the orange curve (Affine JLF), the density used as input in $M2$ is obtained with the affine transformed JLF method. For the green curve (RBF), the density used as input in $M2$ is obtained with RBF density, while in both cases, the floating potentials are obtained with the $M1(V_f)$ model using RBF regression. The parts in lighter color are obtained using data with a 1nA filter, whereas the darker color parts are obtained using data with currents above 10 nA. While the graph only shows currents above 30 nA, the 1 nA filter curve extends to the left down to about 5 nA, however, these calculated +10 volt probe currents plateau in this range and are far from the measured currents. This behavior is likely due to noise levels of about 10 nA, thus extra caution should be taken when using model inferences for data below 10 nA. The RMSr calculated for the 10 nA NorSat-1 current using direct RBF density as $M1(n_e)$ is 9%, and the MRE is 28 %, whereas these numbers for the affine transformed JLF densities are 11 % and 23 %, respectively. The calculated +10 V probe currents based on RBF regression and affine transformed JLF method nicely follow the measured +10 volt probe current except for a small increase in the variance at lower currents, thus indicating that our model constructed with synthetic data set should be applicable to in situ data.

583 5 Conclusions

584 Two new approaches are presented and assessed, to infer plasma and satellite param-
 585 eters from currents measured with multiple fixed bias needle Langmuir probes. In
 586 the first approach, inferences are made with two multivariate regression techniques, con-
 587 sisting of radial basis functions, and neural networks. The second approach relies on a
 588 simple affine transformation combined with a technique first proposed by Jacobsen to
 589 infer the plasma density. Yet another approach, proposed by Barjatya, et al. is consid-
 590 ered, which consists of performing nonlinear fits of measured currents, to an analytic ex-
 591 pression involving the density, the floating potential and the exponent β as fitting pa-
 592 rameters, while the electron temperature is estimated by other means. In all cases, the
 593 accuracy of inferences is assessed on the basis of synthetic data obtained from kinetic
 594 simulations made for space-plasma conditions representative of those encountered along
 595 the NorSat-1 satellite. In addition to assessments based on synthetic data, a consistency
 596 check is presented, whereby densities and satellite potentials inferred from collected cur-
 597 rents, are used as input in an inverse regression model to infer currents for one of the
 598 probes. The advantage of this consistency check is that it is applicable to both synthetic,
 599 and in situ measured currents, and in the latter case, it does not rely on a priori given
 600 inferred densities and satellite potentials. Inference consistency checks are made with
 601 both synthetic and in situ measured currents, showing excellent agreement.

602 The density inference methods considered in this study yield excellent results when
 603 applied to the synthetic data set. The models constructed with synthetic data are then
 604 applied to currents measured by the four m-NLP on NorSat-1. When applied to NorSat-
 605 1 data, the Barjatya nonlinear fit approach is modified by assuming a fixed value for the
 606 temperature and β , and carrying the fit with only the electron density and satellite po-
 607 tential as fitting parameters. The density inferences from all methods show good agree-
 608 ment, confirming that either method should be a significant improvement over the com-
 609 monly used OML approach based on $\beta = 0.5$. From our findings, direct RBF and the
 610 combination of Jacobsen's linear fit with $\beta = 0.5$ with an affine transformation, appear
 611 as being the most promising, and deserving of further study. These two methods pro-
 612 vide inferences that are consistent and quantitatively similar, while being relatively sim-
 613 ple and numerically efficient. The former yields the lowest maximum relative error when
 614 assessed with synthetic data, whereas the latter is the simplest method and produces in-
 615 ferences with comparable accuracy. The spacecraft floating potential is also inferred us-
 616 ing RBF regression, an adapted OML approach and Barjatya nonlinear fit method. The
 617 adapted OML inferences are inconsistent with the measurements from NorSat-1 data since
 618 it indicates that the satellite potential is below -6V, while measurements indicate that
 619 the +6 V probe is collecting electron current. Conversely, spacecraft potentials inferred
 620 with RBF regression, and the nonlinear fit approach yield potentials that are consistent
 621 with measured currents from the +6 V biased probe, showing that the satellite poten-
 622 tial must have been at or above -6 V for most of the one and a half orbital period con-
 623 sidered. This failure to produce acceptable values of the satellite potential using Eq. 14,
 624 and the fact that the Barjatya nonlinear fit approach with n_e , V_f , and β as fitting pa-
 625 rameters, results in β values appreciably larger than one, shows that in situ measure-
 626 ments on NorSat-1 generally do not closely follow the empirical expression in Eq. 1.

627 The analysis presented here has been focused on fixed bias multi-needle Langmuir
 628 probes, with the same dimensions as the ones mounted on NorSat-1, to which it has been
 629 applied as a case study. We stress, however, that the simulation-regression approach to
 630 infer space plasma parameters, is not limited to fixed bias probes or to this particular
 631 configuration of probes. With kinetic solutions capable of reproducing analytic results
 632 under conditions when they are valid, and also capable of accounting for more physics,
 633 and more realistic geometries than theories, solution libraries, training and validation
 634 sets can just as well be constructed for different probes, mounted on satellites, operated
 635 in fixed or sweep bias voltage mode. By following standard machine learning procedures,
 636 whereby models are trained on a subset of a solution library of known independent and
 637 dependent variables, and tested by applying them to distinct subsets, we can estimate

638 uncertainty margins specifically associated with different inference techniques. Another
 639 important strength of the proposed simulation-regression approach is that it enables rel-
 640 atively straightforward incremental improvements to a model, by accounting for more
 641 physical processes or more detailed geometries; something that would be very difficult
 642 to do in a theory. Implementation of regression models and affine transformation of the
 643 Jacobsen linear fit model involve simple arithmetic expressions with pre-calculated co-
 644 efficients and can easily be programmed for onboard processing of low level data. These
 645 approaches, however, would require the creation of custom data sets, when applied to
 646 a given mission, so as to account for the geometry relevant to the measuring instruments,
 647 and the space environment conditions expected along a satellite orbit. In cases where
 648 probe characteristics are well approximated with analytic expressions such as Eq. 1, the
 649 BNLF technique should prove fast and convenient, as it does not require extensive sim-
 650 ulations. Custom simulation-regression models, on the other hand, would require more
 651 computational resources, which would necessitate optimization in order to be implemented
 652 onboard a satellite. Despite their complexity, however, such models would have the ad-
 653 vantage of being more general than models based on fits made with empirical analytic
 654 expressions. The work presented here is by no means final. The development of improved
 655 inference approaches based on simulations and regression techniques will require signif-
 656 icantly more efforts, involving collaborations between experimentalists and modelers; an
 657 effort well worth doing, considering the cost and years of preparation involved in scien-
 658 tific space missions, and the possible scientific payoff.

659 Acknowledgments

660 This work was supported by the China Scholarship Council, the Natural Sciences and
 661 Engineering Research Council of Canada, the Research Council of Norway (Grant Agree-
 662 ment No. 275655 and 325074), and the European Research Council (ERC) under the Eu-
 663 ropean Union’s Horizon 2020 research and innovation program (Grant Agreement No.
 664 866357, POLAR-4DSpace). The kinetic simulations used in this study were made on the
 665 Compute Canada computing infrastructure. S.M. also acknowledges Dag Mortensen, Øyvind
 666 Jensen, and the Institute for Energy Technology for permission to participate in this re-
 667 search.

668 References

- 669 Abadi, M., Barham, P., Chen, J., Chen, Z., Davis, A., Dean, J., ... others (2016).
 670 Tensorflow: A system for large-scale machine learning. In (p. 265-283).
- 671 Allen, J. E., Boyd, R. L. F., & Reynolds, P. (1957, 3). The collection of positive ions
 672 by a probe immersed in a plasma. *Proceedings of the Physical Society. Section*
 673 *B*, 70, 297-304. Retrieved from [https://doi.org/10.1088/0370-1301/70/](https://doi.org/10.1088/0370-1301/70/3/303)
 674 [3/303](https://iopscience.iop.org/article/10.1088/0370-1301/70/3/303)<https://iopscience.iop.org/article/10.1088/0370-1301/70/3/303>
 675 doi: 10.1088/0370-1301/70/3/303
- 676 Barjatya, A., & Merritt, W. (2018). Error analysis of multi-needle langmuir probe
 677 measurement technique. *Review of Scientific Instruments*, 89, 1-5. Retrieved
 678 from <http://dx.doi.org/10.1063/1.5022820> doi: 10.1063/1.5022820
- 679 Barjatya, A., St-Maurice, J. P., & Swenson, C. M. (2013). Elevated electron
 680 temperatures around twin sporadic e layers at low latitude: Observations
 681 and the case for a plausible link to currents parallel to the geomagnetic
 682 field. *Journal of Geophysical Research: Space Physics*, 118, 7316-7328. doi:
 683 10.1002/2013JA018788
- 684 Barjatya, A., Swenson, C. M., Thompson, D. C., & Wright, K. H. (2009). In-
 685 vited article: Data analysis of the floating potential measurement unit aboard
 686 the international space station. *Review of Scientific Instruments*, 80. doi:
 687 10.1063/1.3116085
- 688 Bekkeng, T. A., Jacobsen, K. S., Bekkeng, J. K., Pedersen, A., Lindem, T., Lebre-

- 689 ton, J. P., & Moen, J. I. (2010, 8). Design of a multi-needle langmuir probe
690 system. *Measurement Science and Technology*, *21*, 085903. Retrieved from
691 <https://iopscience.iop.org/article/10.1088/0957-0233/21/8/085903>
692 doi: 10.1088/0957-0233/21/8/085903
- 693 Bernstein, I. B., & Rabinowitz, I. N. (1959). Theory of electrostatic probes in a
694 low-density plasma. *Physics of Fluids*, *2*, 112. Retrieved from [https://aip](https://aip.scitation.org/doi/10.1063/1.1705900)
695 [.scitation.org/doi/10.1063/1.1705900](https://aip.scitation.org/doi/10.1063/1.1705900) doi: 10.1063/1.1705900
- 696 Bhattarai, S., & Mishra, L. N. (2017, 8). Theoretical study of spherical langmuir
697 probe in maxwellian plasma. *International Journal of Physics*, *5*, 73-81.
698 Retrieved from <http://pubs.sciepub.com/ijp/5/3/2/index.html> doi:
699 10.12691/ijp-5-3-2
- 700 Bilitza, D., Altadill, D., Zhang, Y., Mertens, C., Truhlik, V., Richards, P., ...
701 Reinisch, B. (2014, 2). The international reference ionosphere 2012 – a model
702 of international collaboration. *Journal of Space Weather and Space Climate*, *4*,
703 A07. Retrieved from <http://www.swsc-journal.org/10.1051/swsc/2014004>
704 doi: 10.1051/swsc/2014004
- 705 Chalaturnyk, J., & Marchand, R. (2019, 5). Regression-based interpretation of
706 langmuir probe measurements. *Frontiers in Physics*, *7*. Retrieved from
707 <https://www.frontiersin.org/article/10.3389/fphy.2019.00063/full>
708 doi: 10.3389/fphy.2019.00063
- 709 Chen, F. F. (1965, 1). Numerical computations for ion probe characteristics in
710 a collisionless plasma. *Journal of Nuclear Energy. Part C, Plasma Physics,*
711 *Accelerators, Thermonuclear Research*, *7*, 47-67. Retrieved from [https://](https://doi.org/10.1088/0368-3281/7/1/306)
712 doi.org/10.1088/0368-3281/7/1/306[https://iopscience.iop.org/](https://iopscience.iop.org/article/10.1088/0368-3281/7/1/306)
713 [article/10.1088/0368-3281/7/1/306](https://iopscience.iop.org/article/10.1088/0368-3281/7/1/306) doi: 10.1088/0368-3281/7/1/306
- 714 Chen, F. F. (2003). Lecture notes on langmuir probe diagnostics. Mini-Course on
715 Plasma Diagnostics, IEEEICOPS meeting. Retrieved from [http://www.seas](http://www.seas.ucla.edu/~ffchen/Publs/Chen210R.pdf)
716 [.ucla.edu/~ffchen/Publs/Chen210R.pdf](http://www.seas.ucla.edu/~ffchen/Publs/Chen210R.pdf)
- 717 Debchoudhury, S., Barjatya, A., Minow, J. I., Coffey, V. N., & Chandler, M. O.
718 (2021, 10). Observations and validation of plasma density, tempera-
719 ture, and o+ abundance from a langmuir probe onboard the international
720 space station. *Journal of Geophysical Research: Space Physics*, *126*. doi:
721 10.1029/2021JA029393
- 722 Deca, J., Lapenta, G., Marchand, R., & Markidis, S. (2013). Spacecraft charg-
723 ing analysis with the implicit particle-in-cell code iPic3D. *Physics of Plasmas*,
724 *20*(10), 102902. Retrieved from <https://doi.org/10.1063/1.4826951> doi:
725 10.1063/1.4826951
- 726 Ergun, R. E., Andersson, L. A., Fowler, C. M., & Thaller, S. A. (2021, 3). Kinetic
727 modeling of langmuir probes in space and application to the MAVEN langmuir
728 probe and waves instrument. *Journal of Geophysical Research: Space Physics*,
729 *126*. doi: 10.1029/2020JA028956
- 730 Frey, P., & George, P. L. (2007). *Mesh generation: Application to finite elements*.
731 ISTE.
- 732 Geuzaine, C., & Remacle, J.-F. (2009, 9). Gmsh: A 3-D finite element mesh gener-
733 ator with built-in pre- and post-processing facilities. *International Journal for*
734 *Numerical Methods in Engineering*, *79*, 1309-1331. Retrieved from [http://doi](http://doi.wiley.com/10.1002/nme.2579)
735 [.wiley.com/10.1002/nme.2579](http://doi.wiley.com/10.1002/nme.2579) doi: 10.1002/nme.2579
- 736 Goodfellow, I., Bengio, Y., & Courville, A. (2016). *Deep learning*. MIT Press. Re-
737 trieved from <https://books.google.ca/books?id=Np9SDQAAQBAJ>
- 738 Guthrie, J., Marchand, R., & Marholm, S. (2021). Inference of plasma parameters
739 from fixed-bias multi-needle langmuir probes (m-NLP). *Measurement Science*
740 *and Technology*, *32*. doi: 10.1088/1361-6501/abf804
- 741 Hoang, H., Clausen, L. B., Røed, K., Bekkeng, T. A., Trondsen, E., Lybekk, B.,
742 ... Moen, J. I. (2018, 6). The multi-needle langmuir probe system on
743 board NorSat-1. *Space Science Reviews*, *214*, 75. Retrieved from <http://>

- 744 [dx.doi.org/10.1007/s11214-018-0509-2](https://doi.org/10.1007/s11214-018-0509-2)<http://link.springer.com/>
745 [10.1007/s11214-018-0509-2](https://doi.org/10.1007/s11214-018-0509-2) doi: 10.1007/s11214-018-0509-2
- 746 Hoang, H., Røed, K., Bekkeng, T. A., Moen, J. I., Clausen, L. B., Trondsen, E., ...
747 Sagi, E. (2019). The multi-needle langmuir probe instrument for QB50 mis-
748 sion: Case studies of Ex-Altta 1 and hoopoe satellites. *Space Science Reviews*,
749 *215*. Retrieved from <http://dx.doi.org/10.1007/s11214-019-0586-x> doi:
750 [10.1007/s11214-019-0586-x](https://doi.org/10.1007/s11214-019-0586-x)
- 751 Hoang, H., Røed, K., Bekkeng, T. A., Moen, J. I., Spicher, A., Clausen, L. B. N.,
752 ... Pedersen, A. (2018, 6). A study of data analysis techniques for the multi-
753 needle langmuir probe. *Measurement Science and Technology*, *29*, 065906.
754 Retrieved from [https://iopscience.iop.org/article/10.1088/1361-6501/](https://iopscience.iop.org/article/10.1088/1361-6501/aab948)
755 [aab948](https://doi.org/10.1088/1361-6501/aab948) doi: 10.1088/1361-6501/aab948
- 756 Hoskinson, A. R., & Hershkowitz, N. (2006). Effect of finite length on the
757 current-voltage characteristic of a cylindrical langmuir probe in a multidipole
758 plasma chamber. *Plasma Sources Science and Technology*, *15*, 85-90. doi:
759 [10.1088/0963-0252/15/1/013](https://doi.org/10.1088/0963-0252/15/1/013)
- 760 Ivarsen, M. F., Hoang, H., Yang, L., Clausen, L. B., Spicher, A., Jin, Y., ... Lybekk,
761 B. (2019). Multineedle langmuir probe operation and acute probe current
762 susceptibility to spacecraft potential. *IEEE Transactions on Plasma Science*,
763 *47*, 3816-3823. doi: 10.1109/TPS.2019.2906377
- 764 Jacobsen, K. S., Pedersen, A., Moen, J. I., & Bekkeng, T. A. (2010). A new lang-
765 muir probe concept for rapid sampling of space plasma electron density. *Mea-*
766 *surement Science and Technology*, *21*. doi: 10.1088/0957-0233/21/8/085902
- 767 Johnson, J. D., & Holmes, A. J. T. (1990, 10). Edge effect correction for small pla-
768 nar langmuir probes. *Review of Scientific Instruments*, *61*, 2628-2631. doi: 10
769 [.1063/1.1141849](https://doi.org/10.1063/1.1141849)
- 770 Kingma, D. P., & Ba, J. (2015). Adam: A method for stochastic optimization. In
771 Y. Bengio & Y. LeCun (Eds.), . Retrieved from <http://arxiv.org/abs/1412>
772 [.6980](https://doi.org/10.48550/arXiv.1412.6980)
- 773 Laframboise, J. G. (1966). Theory of spherical and cylindrical langmuir probes in
774 a collisionless, maxwellian plasma at rest. *Toronto Univ. (Ontario). Inst. for*
775 *Aerospace Studies*. Retrieved from <https://www.osti.gov/biblio/4522330>
- 776 Lebreton, J.-P., Stverak, S., Travnicsek, P., Maksimovic, M., Klinge, D., Merikallio,
777 S., ... Salaquarda, M. (2006, 4). The ISL langmuir probe experiment
778 processing onboard DEMETER: Scientific objectives, description and
779 first results. *Planetary and Space Science*, *54*, 472-486. Retrieved from
780 <https://linkinghub.elsevier.com/retrieve/pii/S0032063305002084>
781 doi: 10.1016/j.pss.2005.10.017
- 782 Lira, P. A. R., Marchand, R., Burchill, J., & Forster, M. (2019, 8). Deter-
783 mination of Swarm front plate's effective cross section from kinetic sim-
784 ulations. *IEEE Transactions on Plasma Science*, *47*, 3667-3672. Re-
785 trieved from <https://ieeexplore.ieee.org/document/8725927/> doi:
786 [10.1109/TPS.2019.2915216](https://doi.org/10.1109/TPS.2019.2915216)
- 787 Liu, G., & Marchand, R. (2021). Kinetic simulation of segmented plasma flow mer-
788 ter response in the ionospheric plasma. *Journal of Geophysical Research: Space*
789 *Physics*, *126*. doi: 10.1029/2021JA029120
- 790 Liu, G., & Marchand, R. (2022). Inference of m-NLP data using radial basis func-
791 tion regression with center-evolving algorithm. *Computer Physics Commu-*
792 *nications*, *280*, 108497. Retrieved from [https://www.sciencedirect.com/](https://www.sciencedirect.com/science/article/pii/S0010465522002168)
793 [science/article/pii/S0010465522002168](https://doi.org/10.1016/j.cpc.2022.108497) doi: [https://doi.org/10.1016/](https://doi.org/10.1016/j.cpc.2022.108497)
794 [j.cpc.2022.108497](https://doi.org/10.1016/j.cpc.2022.108497)
- 795 Marchand, R. (2012, 2). PTetra, a tool to simulate low orbit satellite-plasma inter-
796 action. *IEEE Transactions on Plasma Science*, *40*, 217-229. Retrieved from
797 <http://ieeexplore.ieee.org/document/6069605/> doi: 10.1109/TPS.2011
798 [.2172638](https://doi.org/10.1109/TPS.2011.2172638)

- 799 Marchand, R., & Lira, P. A. R. (2017, 4). Kinetic simulation of space-
800 craft–environment interaction. *IEEE Transactions on Plasma Science*, *45*,
801 535-554. Retrieved from <http://ieeexplore.ieee.org/document/7888602/>
802 doi: 10.1109/TPS.2017.2682229
- 803 Marchand, R., Miyake, Y., Usui, H., Deca, J., Lapenta, G., Matéo-Vélez, J. C., ...
804 Markidis, S. (2014). Cross-comparison of spacecraft–environment interaction
805 model predictions applied to solar probe plus near perihelion. *Physics of Plas-*
806 *mas*, *21*(6), 062901. Retrieved from <https://doi.org/10.1063/1.4882439>
807 doi: 10.1063/1.4882439
- 808 Marholm, S., & Marchand, R. (2020, 4). Finite-length effects on cylindrical
809 langmuir probes. *Physical Review Research*, *2*, 023016. Retrieved from
810 <https://link.aps.org/doi/10.1103/PhysRevResearch.2.023016> doi:
811 10.1103/physrevresearch.2.023016
- 812 Marholm, S., Marchand, R., Darian, D., Miloch, W. J., & Mortensen, M. (2019,
813 8). Impact of miniaturized fixed-bias multineedle langmuir probes on
814 CubeSats. *IEEE Transactions on Plasma Science*, *47*, 3658-3666. Re-
815 trieved from <https://ieeexplore.ieee.org/document/8734022/> doi:
816 10.1109/TPS.2019.2915810
- 817 Mott-Smith, H. M., & Langmuir, I. (1926). The theory of collectors in gaseous dis-
818 charges. *Physical Review*, *28*, 727-763. doi: 10.1103/PhysRev.28.727
- 819 Olowookere, A., & Marchand, R. (2021). Fixed bias probe measurement of a satellite
820 floating potential. *IEEE Transactions on Plasma Science*, *49*, 862-870. doi: 10
821 .1109/TPS.2020.3045366
- 822 Rudakov, D. L., Boedo, J. A., Moyer, R. A., Lehmer, R. D., Gunner, G., & Watkins,
823 J. G. (2001). Fast electron temperature diagnostic based on langmuir probe
824 current harmonic detection on DIII-D. *Review of Scientific Instruments*, *72*,
825 453-456. doi: 10.1063/1.1310577
- 826 Saad, Y. (2003). *Iterative methods for sparse linear systems* (Second ed.). Society
827 for Industrial and Applied Mathematics. Retrieved from [https://epubs.siam](https://epubs.siam.org/doi/abs/10.1137/1.9780898718003)
828 [.org/doi/abs/10.1137/1.9780898718003](http://epubs.siam.org/doi/book/10.1137/1.9780898718003)[http://epubs.siam.org/doi/](http://epubs.siam.org/doi/book/10.1137/1.9780898718003)
829 [book/10.1137/1.9780898718003](http://epubs.siam.org/doi/book/10.1137/1.9780898718003) doi: 10.1137/1.9780898718003
- 830 Sheridan, T. E. (2010, 3). The plasma sheath around large discs and ion collection
831 by planar langmuir probes. *Journal of Physics D: Applied Physics*, *43*, 105204.
832 doi: 10.1088/0022-3727/43/10/105204
- 833 Sudit, I. D., & Woods, R. C. (1994). A study of the accuracy of various langmuir
834 probe theories. *Journal of Applied Physics*, *76*, 4488-4498. doi: 10.1063/1
835 .357280